Journal of Non-Newtonian Fluid Mechanics 175-176 (2012) 44–54

Contents lists available at SciVerse ScienceDirect

Journal of Non-Newtonian Fluid Mechanics

journal homepage: http://www.elsevier.com/locate/jnnfm

Application of the log-conformation tensor to three-dimensional time-dependent free surface flows

M.F. Tomé [a,*], A. Castelo [a], A.M. Afonso [b], M.A. Alves [b], F.T. Pinho [c]

[a] Departamento de Matemática Aplicada e Estatística, Universidade de São Paulo, Avenida do Trabalhador Saocarlense, 400, 13560-970 São Carlos, SP, Brazil
[b] CEFT, Departamento de Engenharia Química-Faculdade de Engenharia da Universidade do Porto, Rua Dr. Roberto Frias s/n, 4200-465 Porto, Portugal
[c] CEFT, Faculdade de Engenharia da Universidade do Porto, Rua Dr. Roberto Frias s/n, 4200-465 Porto, Portugal

ARTICLE INFO

Article history:
Received 23 August 2011
Received in revised form 10 January 2012
Accepted 20 March 2012
Available online 28 March 2012

Keywords:
Log-conformation tensor
Free surface flows
Finite difference
UCM model
Extrudate swell
Jet buckling

ABSTRACT

The numerical simulation of flows of highly elastic fluids has been the subject of intense research over the past decades with important industrial applications. Therefore, many efforts have been made to improve the convergence capabilities of the numerical methods employed to simulate viscoelastic fluid flows. An important contribution for the solution of the High-Weissenberg Number Problem has been presented by Fattal and Kupferman [J. Non-Newton. Fluid. Mech. 123 (2004) 281–285] who developed the matrix-logarithm of the conformation tensor technique, henceforth called log-conformation tensor. Its advantage is a better approximation of the large growth of the stress tensor that occur in some regions of the flow and it is doubly beneficial in that it ensures physically correct stress fields, allowing converged computations at high Weissenberg number flows. In this work we investigate the application of the log-conformation tensor to three-dimensional unsteady free surface flows. The log-conformation tensor formulation was applied to solve the Upper-Convected Maxwell (UCM) constitutive equation while the momentum equation was solved using a finite difference Marker-and-Cell type method. The resulting developed code is validated by comparing the log-conformation results with the analytic solution for fully developed pipe flows. To illustrate the stability of the log-conformation tensor approach in solving three-dimensional free surface flows, results from the simulation of the extrudate swell and jet buckling phenomena of UCM fluids at high Weissenberg numbers are presented.

1. Introduction

Free surface flows of complex fluids are important in the polymer processing industry, the typical application being the extrusion process of a polymer melt. In this process, a polymer melt is forced to flow through a die using a piston and the deformation of the polymer as it exits the die eventually determines the final shape of the extrudate. Hence, accurate simulation of the complex flow along the die and at the exit is extremely important in order to properly design the shape of the die that produces the extrudate with the desired prescribed shape [22]. After exiting the die the fluid usually swells to an extent that is strongly dependent on the fluid rheology and on the stress conditions, which depends on the flow history inside the die. For this reason, the inverse problem of finding the correct die shape that produces the desired extrudate profile [22] is of paramount importance in the polymer processing industry. On the other hand, increasing the production rate often leads to the onset of elastic-driven flow instabilities, and the surface of the extrudate looses the desired smoothness. This sharkskin instability arises at high flow rates, and at more extreme conditions melt fracture may occur. These instabilities are undesirable and have a negative impact on the quality of the produced extrudate [17]. Accurate modelling of the flow in these complex geometries can have a critical role in the optimisation of the operational parameters, namely the productivity of the extrusion process.

In this work we study numerically the flow at the exit of a circular tube, known as the die-swell problem (or more accurately called extrudate swell), aiming at quantifying the swell ratio as a function of the Weissenberg number (*Wi*), for a fluid that is described by the Upper-Convected Maxwell (UCM) constitutive equation . Due to the discontinuity of the tube wall at the die exit, the stress and pressure fields are singular at the exit of the tube [19]. This singular behaviour is difficult to model and typically the maximum Weissenberg number where convergence is achieved is modest, of the order of one for UCM fluids. This inability to simulate viscoelastic flows at high *Wi* has been the major challenge in computational rheology for the last three decades [21] and is known as the High Weissenberg Number Problem (HWNP) [26]. Numerical simulation of different viscoelastic flows suggests that this breakdown in

* Corresponding author. Tel.: +55 16 3373 9656; fax: +55 16 3373 9651.
E-mail addresses: murilo@icmc.usp.br (M.F. Tomé), castelo@icmc.usp.br (A. Castelo), aafonso@fe.up.pt (A.M. Afonso), mmalves@fe.up.pt (M.A. Alves), fpinho@fe.up.pt (F.T. Pinho).

0377-0257/$ - see front matter © 2012 Elsevier B.V. All rights reserved.
http://dx.doi.org/10.1016/j.jnnfm.2012.03.009

numerical stability is related to the emergence of large stress gradients. This may be related to the unsuitability of polynomial-based interpolation schemes, used to calculate stress profiles, to perform well in regions of high shear rates or near stagnation points where the stresses exhibit exponential growth [18] eventually leading to unphysical stress values. A remarkable breakthrough for solving the HWNP was proposed by Fattal and Kupferman [18], known as the log-conformation tensor approach. According to this methodology, an evolution equation for the logarithm of the conformation tensor is solved, reducing the large gradients of the stress and conformation tensor fields. This new logarithm of the conformation tensor technique approximates numerically the stresses with better accuracy in problematic flow regions, where the stress field has an exponential growth. In addition, by construction, the positive definiteness of the conformation tensor is guaranteed no matter the accuracy of the computed solution for the logarithm of the conformation tensor, thus avoiding unphysical stress values. More recently, Afonso et al. [3] proposed a generic matrix transformation for the conformation tensor known as the kernel-conformation tensor transformation.

Over the last 8 years several authors have implemented the log-conformation tensor in their viscoelastic codes (e.g. [1,10,16,18, 21,23,27]) to study confined flows. The application of the log-conformation tensor to free surface flows has recently been considered by Baltussen et al. [5] and Choi and Hulsen [8]. In these works, two-dimensional fountain flow and extrudate swell were investigated. In all cases an enhancement of the stability of the numerical method has been reported, demonstrating the advantage of the log-conformation tensor approach. In this work we describe the implementation of the log-conformation tensor in a finite-difference method used to calculate three-dimensional unsteady free surface flows of viscoelastic fluids. To assess its impact upon the stability and accuracy of the numerical solutions obtained, the flow produced by an impinging jet and the die-swell benchmark flow of a viscoelastic fluid described by the UCM constitutive equation are solved.

The remainder of this paper is organised as follows: in Section 2 we present the governing equations and the log-conformation methodology; in Section 3 we briefly describe the numerical method and proceed to the presentation of the numerical results of the three-dimensional unsteady extrudate swell and jet buckling of an UCM fluid; Section 5 ends the paper with a brief summary of the results.

2. Governing equations

The governing equations for incompressible flows are the mass conservation equation and the equation of motion which, in nondimensional form, can be written as [38]

$$\nabla \cdot \mathbf{u} = 0, \tag{1}$$

$$\frac{\partial \mathbf{u}}{\partial t} + (\mathbf{u}\cdot\nabla)\mathbf{u} = -\nabla p + \frac{1}{Re}\nabla^2\mathbf{u} + \nabla\cdot\mathbf{S} + \frac{1}{Fr^2}\mathbf{g}. \tag{2}$$

In this work the fluid is described by the UCM model which leads to the following equation for the extra-stress tensor $\mathbf{T}$ [37]:

$$\mathbf{T} + Wi\overset{\nabla}{\mathbf{T}} = \frac{2}{Re}\mathbf{D}. \tag{3}$$

The extra-stress $\mathbf{T}$ is decomposed following the EVSS transformation [30] into the sum of an elastic stress tensor $\mathbf{S}$ and a purely viscous contribution

$$\mathbf{T} = \frac{2}{Re}\mathbf{D} + \mathbf{S}, \tag{4}$$

which has already been used in the formulation of the momentum Eq. (2). Additionally, in the equations above, t is the time, $\mathbf{u}$ is the velocity vector, p is the pressure, $\mathbf{g}$ is the gravitational field, λ is the relaxation time of the fluid and $\mathbf{D} = 1/2((\nabla\mathbf{u}) + (\nabla\mathbf{u})^{\mathrm{T}})$ is the rate of deformation tensor. The nondimensional numbers Re, Fr, Wi are, respectively, the Reynolds, Froude and Weissenberg numbers, given by

$$Re = \frac{\rho UL}{\eta_0}; \quad Fr = \frac{U}{\sqrt{gL}}; \quad Wi = \lambda\frac{U}{L},$$

where L and U are length and velocity scales for normalisation, to be defined later when describing the flow geometry and η_0 is the zero shear rate viscosity of the fluid. The flows investigated in this work are at $Re = O(1)$, so we opted to use ρU^2 to normalise stresses and pressure, which is also consistent with previous papers on free surface flows of viscoelastic fluids [28,37,38]. The symbol $(\overset{\nabla}{\cdot})$ represents the upper-convected derivative defined by

$$\overset{\nabla}{\boldsymbol{\phi}} = \frac{\partial \boldsymbol{\phi}}{\partial t} + (\mathbf{u}\cdot\nabla)\boldsymbol{\phi} - (\nabla\mathbf{u})^{\mathrm{T}}\boldsymbol{\phi} - \boldsymbol{\phi}(\nabla\mathbf{u}). \tag{5}$$

Alternatively, the constitutive law (3) can be formulated in terms of the conformation tensor $\mathbf{A}$, which for the UCM fluid is related to $\mathbf{T}$ according to,

$$\mathbf{T} = \frac{1}{ReWi}(\mathbf{A} - \mathbf{I}) \tag{6}$$

where $\mathbf{I}$ is the unitary tensor. The conformation tensor $\mathbf{A}$ is described by an appropriate evolution equation, which for the UCM model is given by [18]

$$\frac{\partial \mathbf{A}}{\partial t} + (\mathbf{u}\cdot\nabla)\mathbf{A} - (\nabla\mathbf{u})^{\mathrm{T}}\mathbf{A} - \mathbf{A}(\nabla\mathbf{u}) = \frac{1}{Wi}(\mathbf{I} - \mathbf{A}). \tag{7}$$

To solve (7) we decompose the velocity gradient transpose as [18]:

$$(\nabla\mathbf{u})^T = \boldsymbol{\Omega} + \mathbf{B} + \mathbf{N}\mathbf{A}^{-1}, \tag{8}$$

where the tensors $\boldsymbol{\Omega}$ and $\mathbf{N}$ are anti-symmetric and the tensor $\mathbf{B}$ is symmetric, traceless and commutes with $\mathbf{A}$. The tensor $\mathbf{B}$ generates a pure (area preserving) extension, while $\boldsymbol{\Omega}$ is responsible for rotations. Substituting the decomposition (8) into equation (7), one finds that the term $\mathbf{N}\mathbf{A}^{-1}$ cancels by anti-symmetry and the following transformed evolution equation for the conformation tensor (see Fattal and Kupferman [18] for details) is obtained

$$\frac{\partial \mathbf{A}}{\partial t} + (\mathbf{u}\cdot\nabla)\mathbf{A} - (\boldsymbol{\Omega}\mathbf{A} - \mathbf{A}\boldsymbol{\Omega}) - 2\mathbf{B}\mathbf{A} = \frac{1}{Wi}(\mathbf{I} - \mathbf{A}). \tag{9}$$

2.1. The log-conformation representation

The log-conformation representation can be obtained by replacing Eq. (9) with an equivalent equation for the tensor

$$\boldsymbol{\Psi} = \log(\mathbf{A}). \tag{10}$$

A Symmetric Positive Definite (SPD) matrix can always be diagonalized so we can find a matrix $\mathbf{R}$ and a diagonal matrix $\boldsymbol{\Lambda}$ so that $\mathbf{A} = \mathbf{R}\boldsymbol{\Lambda}\mathbf{R}^{\mathrm{T}}$. Matrix $\mathbf{R}$ is an orthogonal matrix whose columns are composed by the three eigenvectors of $\mathbf{A}$, whereas the corresponding eigenvalues form the diagonal matrix $\boldsymbol{\Lambda}$. Thus, $\log(\mathbf{A}) = \mathbf{R}\log(\boldsymbol{\Lambda})\mathbf{R}^{\mathrm{T}}$. The transformation from Eq. (9) to an evolution equation for $\boldsymbol{\Psi} = \log(\mathbf{A})$ is straightforward (see Fattal and Kupferman [18] for details) and leads to

$$\frac{\partial \boldsymbol{\Psi}}{\partial t} + (\mathbf{u}\cdot\nabla)\boldsymbol{\Psi} - (\boldsymbol{\Omega}\boldsymbol{\Psi} - \boldsymbol{\Psi}\boldsymbol{\Omega}) - 2\mathbf{B} = \frac{1}{Wi}(\mathbf{e}^{-\boldsymbol{\Psi}} - \mathbf{I}). \tag{11}$$

Therefore, we need to solve Eqs. (1), (2) and (11) together with Eqs. (10), (6) and (4) to determine $\mathbf{u}$, p, $\boldsymbol{\Psi}$, $\mathbf{A}$, $\mathbf{T}$ and $\mathbf{S}$, respectively.

2.2. Boundary conditions

In order to solve Eqs. (1) and (2) it is necessary to impose boundary conditions for the velocity field on mesh boundaries.

For rigid boundaries we employ the no-slip condition $\mathbf{u} = \mathbf{0}$ while at fluid entrances (inflows) the normal velocity is specified by $U_n = U_{in}$ and the tangential velocities are set to zero, namely, $U_{m_1} = U_{m_2} = 0$, where m_1 and m_2 denote tangential directions to the inflow plane. At fluid exits (outflows) the Neumann condition $\frac{\partial \mathbf{u}}{\partial n} = \mathbf{0}$ is adopted. We consider a viscous fluid flowing in a passive atmosphere and surface tension forces are neglected at the liquid–gas interface. Then, on the liquid free surface the correct boundary conditions are given by (see Batchelor [4], p. 153)

$$\mathbf{n}^T \cdot (\boldsymbol{\sigma} \cdot \mathbf{n}) = 0, \tag{12}$$

$$\mathbf{m}_1^T \cdot (\boldsymbol{\sigma} \cdot \mathbf{n}) = 0, \tag{13}$$

$$\mathbf{m}_2^T \cdot (\boldsymbol{\sigma} \cdot \mathbf{n}) = 0, \tag{14}$$

where $\mathbf{n}$ is the outward unit normal vector to the free surface and $\mathbf{m_1}$, $\mathbf{m_2}$ are unit tangential vectors and $\boldsymbol{\sigma}$ is the total stress tensor which can be written as $\boldsymbol{\sigma} = -p\mathbf{I} + \frac{2}{Re}\mathbf{D} + \mathbf{S}$.

3. Numerical method

The method of solution is based on the projection method introduced by Chorin [9] (for projection methods used within a finite element framework see Guermond and Quatapelle [20]).

To solve Eqs. (1), (2), (11), (10) and (6) together with the equations defining the boundary conditions we use the methodology employed by Tomé et al. [38] for three-dimensional viscoelastic free surface flows governed by the Oldroyd-B model.

Suppose that $\mathbf{u}(\mathbf{x}, t_n)$, $\mathbf{T}(\mathbf{x}, t_n)$ are known and boundary conditions for velocity and pressure are given. Then, $\mathbf{u}(\mathbf{x}, t_{n+1})$, $p(\mathbf{x}, t_{n+1})$, $\boldsymbol{\Psi}(\mathbf{x}, t_{n+1})$, $\mathbf{A}(\mathbf{x}, t_{n+1})$ and $\mathbf{T}(\mathbf{x}, t_{n+1})$, where $t_{n+1} = t_n + \delta t$, can be obtained as follows:

Step 1: Using the known velocity field at time t_n, $\mathbf{u}(\mathbf{x}, t_n)$, compute the rate-of-deformation tensor $\mathbf{D}(\mathbf{x}, t_n)$ and then calculate the non-Newtonian tensor $\mathbf{S}(\mathbf{x}, t_n)$ from the EVSS transformation Eq. (4).

Step 2: Let $\tilde{p}(\mathbf{x}, t_n)$ be a pressure field which satisfies the correct pressure condition on the free surface. This pressure field is computed so that the normal stress condition (12) is satisfied. In the Freeflow3D code, $\tilde{p}(\mathbf{x}, t_n)$ is computed by setting $\tilde{p}(\mathbf{x}, t_n) = p(\mathbf{x}, t_n)$ in full cells. In surface cells, the pressure is calculated by equation $\mathbf{n}^T \cdot \boldsymbol{\sigma} \cdot \mathbf{n} = 0$ (since surface tension was neglected, see Batchelor [4], p. 153). More especifically, $\tilde{p}(\mathbf{x}, t_n)$ is calculated from equation

$$\begin{aligned}\tilde{p} = \frac{2}{Re}\Bigg[&\frac{\partial u}{\partial x}n_x^2 + \frac{\partial v}{\partial y}n_y^2 + \frac{\partial w}{\partial z}n_z^2 + \left(\frac{\partial v}{\partial x} + \frac{\partial u}{\partial y}\right)n_x n_y \\ &+ \left(\frac{\partial w}{\partial x} + \frac{\partial u}{\partial z}\right)n_x n_z + \left(\frac{\partial w}{\partial y} + \frac{\partial v}{\partial z}\right)n_y n_z\Bigg] \\ &+ S^{xx}n_x^2 + S^{yy}n_y^2 + S^{zz}n_z^2 + 2\left(S^{xy}n_x n_y + S^{xz}n_x n_z + S^{yz}n_y n_z\right).\end{aligned} \tag{15}$$

Details on how this equation is dealt with are provided in Refs. [37–39].

Step 3: Compute the intermediate velocity field, $\tilde{\mathbf{u}}(\mathbf{x}, t_{n+1})$:

$$\frac{\partial \tilde{\mathbf{u}}}{\partial t} = -(\mathbf{u} \cdot \nabla)\mathbf{u} - \nabla\tilde{p} + \frac{1}{Re}\nabla^2\mathbf{u} + \nabla \cdot \mathbf{S} + \frac{1}{Fr^2}\mathbf{g}, \tag{16}$$

with $\tilde{\mathbf{u}}(\mathbf{x}, t_n) = \mathbf{u}(\mathbf{x}, t_n)$ using the correct boundary conditions for $\mathbf{u}(\mathbf{x}, t_n)$. These equations are solved by a finite difference method which is integrated explicitly in time.

Step 4: Solve the Poisson equation

$$\nabla^2\psi(\mathbf{x}, t_{n+1}) = \nabla \cdot \tilde{\mathbf{u}}(\mathbf{x}, t_{n+1}), \tag{17}$$

subject to the following boundary conditions [40]:

$$\frac{\partial \psi}{\partial n} = 0 \text{ on rigid boundaries and inflows and}$$
$$\psi = 0 \text{ on the free surface and outflows.}$$

Step 5: Correct the velocity field to satisfy continuity

$$\mathbf{u}(\mathbf{x}, t_{n+1}) = \tilde{\mathbf{u}}(\mathbf{x}, t_{n+1}) - \nabla\psi(\mathbf{x}, t_{n+1}). \tag{18}$$

Step 6: Compute the pressure field

$$p(\mathbf{x}, t_{n+1}) = \tilde{p}(\mathbf{x}, t_n) + \frac{\psi(\mathbf{x}, t_{n+1})}{\delta t}. \tag{19}$$

Step 7: Decompose the velocity gradient as $\nabla\mathbf{u}(\mathbf{x}, t_{n+1}) = \boldsymbol{\Omega} + \mathbf{B} + \mathbf{N}\mathbf{A}^{-1}$ to determine $\boldsymbol{\Omega}$ and $\mathbf{B}$, details in [18].

Step 8: Using $\mathbf{T}(\mathbf{x}, t_n)$ calculate the conformation tensor $\mathbf{A}(\mathbf{x}, t_n)$ from

$$\mathbf{A}(\mathbf{x}, t_n) = ReWi\mathbf{T}(\mathbf{x}, t_n) + \mathbf{I}. \tag{20}$$

Step 9: Calculate tensors $\mathbf{R}^{(n)}$ and $\boldsymbol{\Lambda}^{(n)}$such that

$$\mathbf{A}(\mathbf{x}, t_n) = \mathbf{R}^{(n)}\boldsymbol{\Lambda}^{(n)}(\mathbf{R}^{(n)})^{\mathrm{T}}$$

and then compute
$\boldsymbol{\Psi}(\mathbf{x}, t_n) = \log(\mathbf{A}(\mathbf{x}, t_n)) = \mathbf{R}^{(n)}\log(\boldsymbol{\Lambda}^{(n)})$
$(\mathbf{R}^{(n)})^{\mathrm{T}}$ and $\mathbf{e}^{-\boldsymbol{\Psi}(\mathbf{x}, t_n)} = (\mathbf{R}^{(n)})(\boldsymbol{\Lambda}^{(n)})^{-1}(\mathbf{R}^{(n)})^{\mathrm{T}}$.

Step 10: Calculate $\boldsymbol{\Psi}(\mathbf{x}, t_{n+1})$ from

$$\begin{aligned}\boldsymbol{\Psi}(\mathbf{x}, t_{n+1}) = \boldsymbol{\Psi}(\mathbf{x}, t_n) + \delta t\Big\{&-(\mathbf{u}(\mathbf{x}, t_{n+1}) \cdot \nabla)\boldsymbol{\Psi}(\mathbf{x}, t_n) \\ &+ [\boldsymbol{\Omega}\boldsymbol{\Psi}(\mathbf{x}, t_n) - \boldsymbol{\Psi}(\mathbf{x}, t_n)\boldsymbol{\Omega}] + 2\mathbf{B} \\ &+ \frac{1}{Wi}(\mathbf{e}^{-\boldsymbol{\Psi}(\mathbf{x}, t_n)} - \mathbf{I})\Big\}.\end{aligned} \tag{21}$$

Step 11: Calculate tensors $\mathbf{R}^{(n+1)}$ and $\boldsymbol{\Lambda}^{(n+1)}$ such that

$$\boldsymbol{\Psi}(\mathbf{x}, t_{n+1}) = \mathbf{R}^{(n+1)}\log(\boldsymbol{\Lambda}^{(n+1)})(\mathbf{R}^{(n+1)})^{\mathrm{T}}. \tag{22}$$

Step 12: The conformation tensor $\mathbf{A}(\mathbf{x}, t_{n+1})$ is calculated by

$$\mathbf{A}(\mathbf{x}, t_{n+1}) = \mathbf{e}^{\boldsymbol{\Psi}(\mathbf{x}, t_{n+1})} = \mathbf{R}^{(n+1)}\boldsymbol{\Lambda}^{(n+1)}(\mathbf{R}^{(n+1)})^{\mathrm{T}}. \tag{23}$$

Step 13: Finally, the extra-stress tensor $\mathbf{T}(\mathbf{x}, t_{n+1})$ is obtained from

$$\mathbf{T}(\mathbf{x}, t_{n+1}) = \frac{1}{ReWi}[\mathbf{A}(\mathbf{x}, t_{n+1}) - \mathbf{I}]. \tag{24}$$

Step 14: Update the positions of the marker particles. The last step in the calculation is to move the markers to their new positions by solving the pure advective differential equation

$$\frac{d\mathbf{x}}{dt} = \mathbf{u}(\mathbf{x}, t_{n+1}), \tag{25}$$

for each particle. The fluid surface is defined by piecewise linear surfaces composed of triangular and quadrilateral shapes with these marker particles at their vertices. Details of particle movement are given in Tomé et al. [39].

We observe that in *Steps 9 and 11* above, it is necessary to compute the eigenvalues and their associated eigenvectors of the conformation tensor $\mathbf{A}$ (a 3×3 symmetric matrix). In the Freeflow3D code, this task has been efficiently performed by the Jacobi iterative algorithm presented in the book of Press et al. [29] with the same procedure being used for full and surface cells.

3.1. Finite difference solution

We consider three-dimensional free surface flows and solve the equations described in *Step 1* to *Step 14* by the finite difference method on a staggered grid (see Fig. 1a). In order to follow the moving free surface, a scheme to define the cells within the mesh

is employed. The cells within the mesh are of different type: empty cells (E or blank cells in Fig. 1b) (cells that do not contain fluid), full cells (F) (cells that contain fluid and are not in contact with empty cells), surface cells (S) (cells that contain fluid and necessarily share one or more faces with empty cells), inflow cells (I) (cells that define an inflow boundary), outflow cells (O) (cells that define an outflow boundary) and boundary cells (B) (cells that define a rigid boundary). Fig. 1b illustrates the type of cells within the mesh for the 2D case.

The finite difference equations corresponding to *Step 1* to *Step 5* can be found in Tomé et al. [38] and so they are not presented here. The left hand side of the Poisson equation (17) is approximated by the Laplacian operator and is applied at every full cell in the domain. This originates a Symmetric Positive Definite linear system which is solved by the conjugate gradient method subject to a tolerance $EPS = 10^{-10}$. *Step 6* to *Step 8* and *Step 10* to *Step 12* contain only products of matrices which are easily computed. The diagonalisation of tensor **A** involves the calculation of the eigenvalues and eigenvectors of **A** at every full and surface cell. The calculation of $\boldsymbol{\Psi}$ in *Step 9* is easily performed using finite differences. The value of $\boldsymbol{\Psi}$ at cell faces required to evaluate the convective term $(\mathbf{u}(\mathbf{x},t_{n+1})\cdot\nabla)\boldsymbol{\Psi}(\mathbf{x},t_n)$ in Eq. (21), is approximated using the high resolution CUBISTA scheme [2].

4. Validations results

In order to simulate free surface flows governed by the UCM constitutive equation employing the log-conformation tensor, the equations described in the previous sections were embodied into the Freeflow3D code [6]. To assess the correctness of the log-conformation tensor in solving the UCM model, we employed the code to simulate the fully developed flow in a 3D pipe of radius R and length $10R$ and compared the corresponding analytic and numerical solutions. We considered the following dimensionless velocity profile at the pipe entrance

$$w(x,y) = 2[1-(x^2+y^2)], \tag{26}$$

where the bulk velocity and pipe radius were used in the normalisation of the velocity and coordinates, respectively. Thus, introducing this profile into the UCM constitutive equation it can be easily verified that one obtains the following analytic solution for the components of the extra-stress tensor:

$$\begin{aligned} &T^{xx}(x,y) = T^{yy}(x,y) = T^{xy}(x,y) = 0,\\ &T^{xz}(x,y) = \frac{1}{Re}\frac{\partial w}{\partial x} = \frac{-4}{Re}x, \quad T^{yz}(x,y) = \frac{1}{Re}\frac{\partial w}{\partial y} = \frac{-4}{Re}y \end{aligned} \tag{27}$$

and

$$T^{zz}(x,y) = 2\frac{Wi}{Re}\left[\left(\frac{\partial w}{\partial x}\right)^2 + \left(\frac{\partial w}{\partial y}\right)^2\right]. \tag{28}$$

On the pipe exit and on the pipe walls, appropriate conditions for the velocity were imposed (see Section 2.2) while for the non-Newtonian stress tensor **T**, the analytic solutions given by Eqs. (27) and (28) were imposed at the pipe entrance (inflow). See Fig. 2.

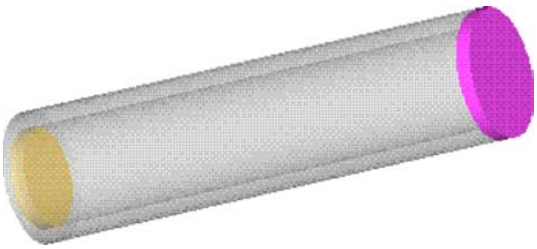

Fig. 2. Illustration of the domain used for the simulation of the flow in a pipe. The yellow and pink objects denote, respectively, inflow and outflow boundaries.

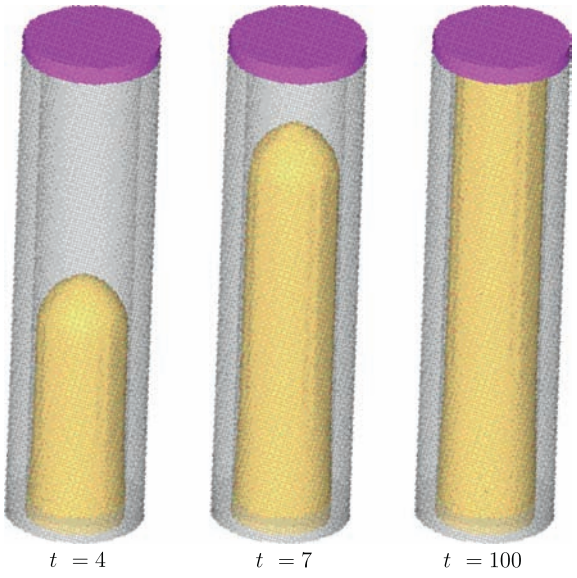

Fig. 3. Numerical simulation of pipe flow, $Re = 1$, $Wi = 1$. Fluid flow visualisation at dimensionless times $t = t^*\frac{U}{R} = 4, 7, 100$. Results obtained on mesh **M2**.

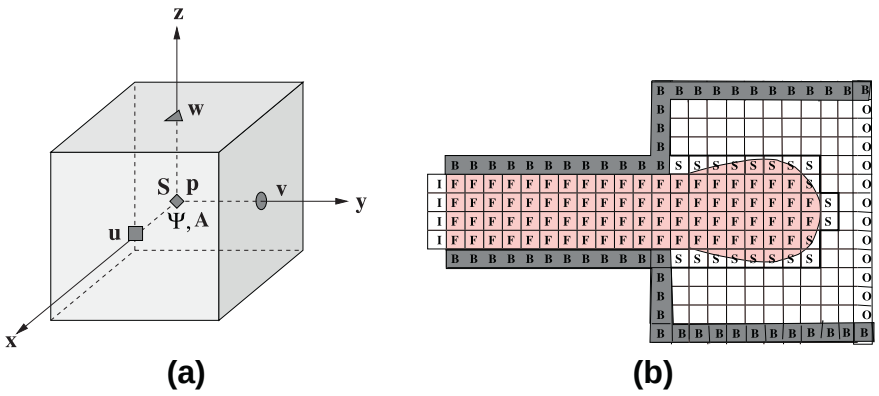

Fig. 1. (a) Three-dimensional staggered grid used; (b) types of cells within the mesh (blank cells denote empty cells).

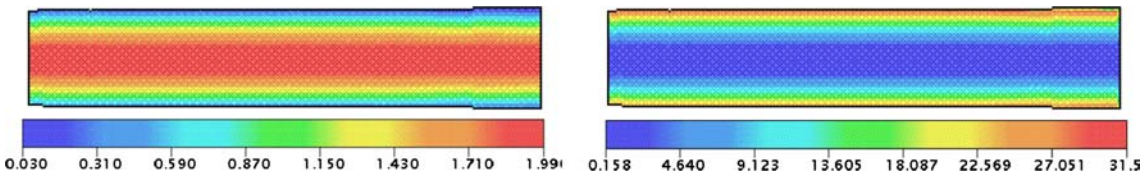

Fig. 4. Contour plots of w and T^{zz} along the pipe at dimensionless time $t = 100$. Results shown on the plane $y = 0$, $0 \leqslant z \leqslant 10$, $-1 \leqslant x \leqslant 1$. Results obtained on mesh **M2**.

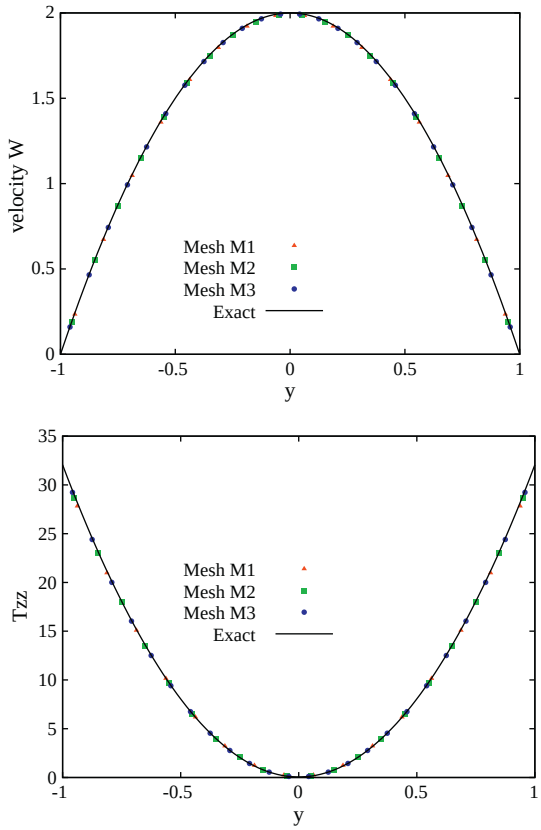

Fig. 5. Numerical simulation of 3D pipe flow at $Re = 1$ and $Wi = 1$. Numerical and analytic solutions at $z = 5$, $x = 0$ and $-1 \leqslant y \leqslant 1$.

Fig. 6. Numerical simulation of extrudate swell with $Re = 0.5$ and $Wi = 0.3$ using the log-conformation tensor (red curve) and the extra-stress tensor (green curve). Visualisation of the free surfaces at dimensionless times $t = t^* \frac{U}{R} = 12.5, 15, 17.5, 20$.

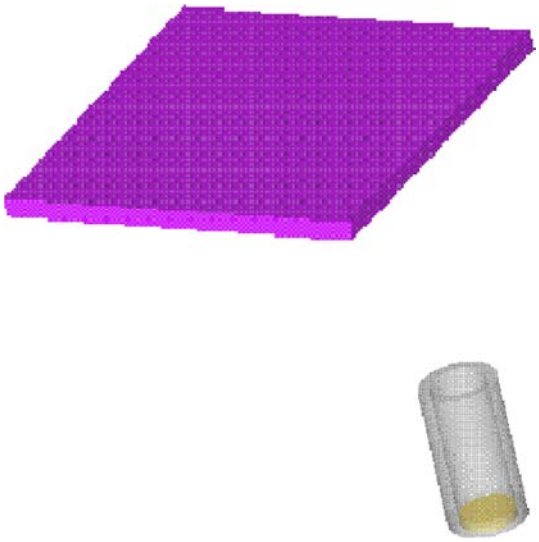

Fig. 7. Domain used for the simulation of the transient extrudate swell. The yellow surface represents the pipe entrance, where an inflow boundary is defined, while the pink surface represents the region where an outflow boundary was set. The grey surface represents the pipe wall. Pipe radius: R; pipe length: $10R$; distance between pipe exit and outflow: $10R$.

Table 1
Errors obtained, at the cross section $z = 5$, on three meshes, using the L_2-norm.

Mesh	**M1**	**M2**	**M3**
$E(w)$	2.6677×10^{-3}	1.6093×10^{-3}	1.0751×10^{-3}
$E(T^{xz})$	2.7903×10^{-3}	1.7036×10^{-3}	1.3108×10^{-3}
$E(T^{yz})$	2.7777×10^{-3}	1.7043×10^{-3}	1.3075×10^{-3}
$E(T^{zz})$	1.0548×10^{-2}	6.6425×10^{-3}	4.8879×10^{-3}

The following input data were employed: $Re = \frac{\rho UR}{\mu} = 1$ and $Wi = \frac{\lambda U}{R} = 1$. In order to demonstrate the convergence of the method, mesh refinement was performed with mesh sizes $\delta x = \delta y = \delta z = 1/8$ (mesh **M1**, $16 \times 16 \times 80$ cells), $\delta x = \delta y = \delta z = 1/10$ (mesh **M2**, $20 \times 20 \times 100$ cells) and $\delta x = \delta y = \delta z = 1/12$ (mesh **M3**, $24 \times 24 \times 120$ cells), respectively.

The simulations started with the pipe empty and the fluid was injected at the inflow. Initially, there was a transient free surface flow inside the pipe; after some time the pipe was completely full and steady state was established (see Fig. 3). Under steady state flow conditions, the velocity and the stress fields, at any cross section of the pipe, must have the same values as those imposed at the inflow.

Fig. 4 shows contour lines of the velocity w and the component T^{zz} of the extra-stress tensor at dimensionless time $t = 100$. We can see that the contour lines are all parallel indicating that the steady state has been established.

The numerical solutions obtained on meshes **M1**, **M2** and **M3** for the velocity w and for the component of the non-Newtonian tensor T^{zz} at the cross section at the middle of the pipe ($z = 5$) are shown in Fig. 5. We can see that there is good agreement between the numerical solutions obtained on the three meshes and the exact solutions, validating the numerical technique presented in this paper. In addition, Table 1 presents the errors obtained on the three meshes using the L_2-norm:

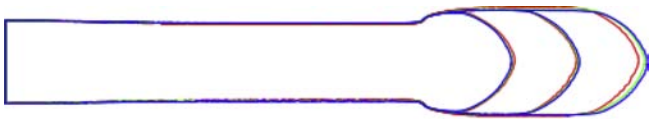

Fig. 8. Numerical simulation of extrudate swell with $Re = 0.5$ and $Wi = 0.3$ using the log-conformation tensor at dimensionless times $t = t^* \frac{U}{R} = 11, 13.5, 16$ using meshes **M1** (red surface), **M2** (green surface), **M3** (blue surface).

$$E = \sqrt{\frac{\sum_{ij}(Ex\ Sol - Num\ Sol)^2}{\sum_{ij}(Ex\ Sol)^2}}. \tag{29}$$

We can see in Table 1 that the errors decrease as the mesh is refined. This fact shows that the numerical method is convergent.

To verify the correctness of the log-conformation implementation for solving free surface problems, the Freeflow3D code was

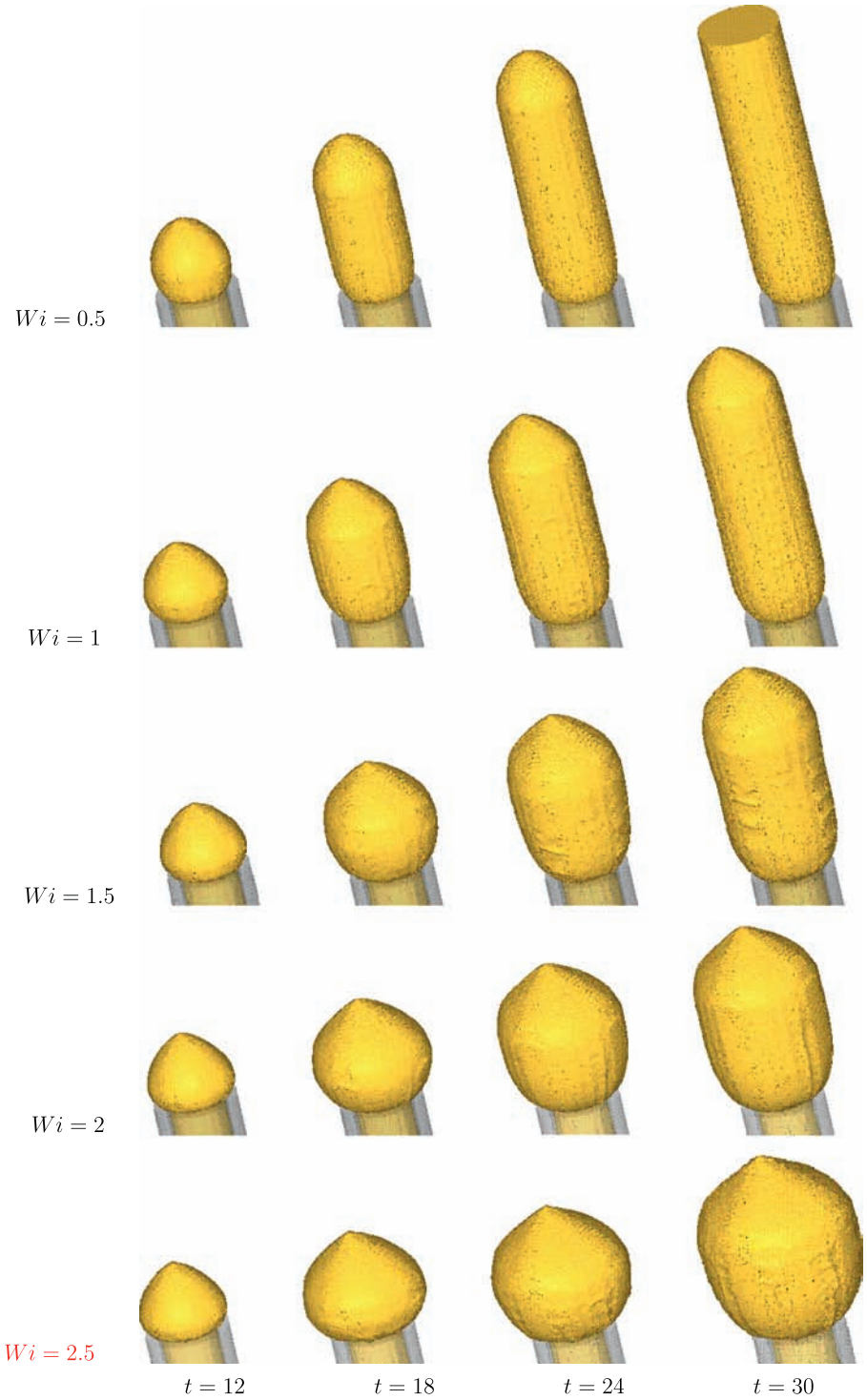

Fig. 9. Numerical simulation of time dependent extrudate swell using the log-conformation tensor technique: $Re = 0.5$, and $Wi = 0.5, 1, 1.5, 2, 2.5$. Fluid flow visualisation at selected dimensionless times. At time $t = 30$, the jet with $Wi = 0.5$ has reached the outflow boundary (not shown).

Table 2
Effect of the Weissenberg number on the swell ratio.

Wi	0.5	0.8	1	1.25	1.5	1.75	2	2.3	2.5
Sr	1.38	1.49	1.58	1.78	1.92	2.00	2.14	2.27	2.37

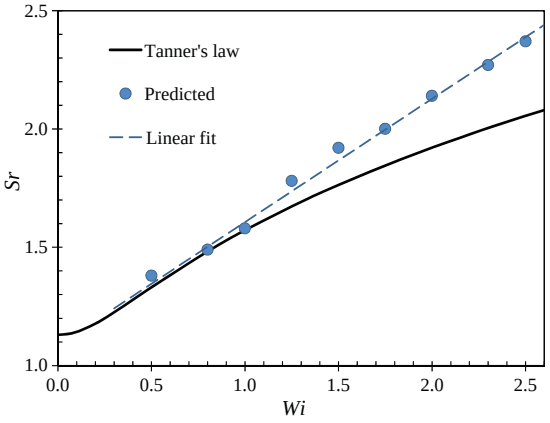

Fig. 10. Numerical simulation of time-dependent extrudate swell for $Re = 0.5$ and $W_i \leqslant 2.5$. Comparison between the *Sr* obtained with the log-conformation tensor approach and Tanner' law [35,36] for creeping flow.

applied to simulate the time-dependent extrudate swell problem and the results obtained were compared with those from the extra-stress tensor UCM3D solver of Tomé et al. [37]. These simulations were performed on mesh **M2** and used $Re = 0.5$ and $Wi = 0.3$. The input data file employed in these simulations was the same for both log-conformation and extra-stress tensor solvers. Fig. 6 presents a comparison of the free surfaces obtained by both codes at selected times. It can be observed that the results from both techniques are similar and qualitatively display equal swelling ratios. However, the shape of the front of the jet is smoother for the log-conformation technique than for the standard formulation. This is compatible with observations that computations of free surface flow of UCM fluids with the standard technique are very unstable.

5. Numerical simulation of three-dimensional time-dependent free surface flows

To illustrate that the log-conformation tensor can cope with high Weissenberg number viscoelastic free surface flows we applied it to simulate the extrudate swell and the jet buckling of UCM fluids as follows.

5.1. Simulation of unsteady extrudate swell

We considered the flow produced by a viscoelastic fluid jet as it emerges from a tube flowing into the air where, it presents the phenomenon known as extrudate swell (it is also referenced as 'die swell'). This problem has practical industrial applications and has been studied by many authors. For example, Tanner [35] presented a theory for obtaining swelling ratios while various authors have numerically investigated the extrudate swell using the Oldroyd-B model, see for example Crochet and Keunings [13], Clermont and Normandin [7], Cormenzana et al. [11], Ngamaramvaranggul and Webster [24], Tomé et al. [38], to mention only a few.

Fig. 11. Numerical simulation of extrudate swell with $Re = 0.5$ and $Wi = 1.5$ using the log-conformation tensor at dimensionless times $t = t^* \frac{U}{R} = 12, 17, 22$ using meshes **M1** (red surface), **M2** (green surface), **M3** (blue surface).

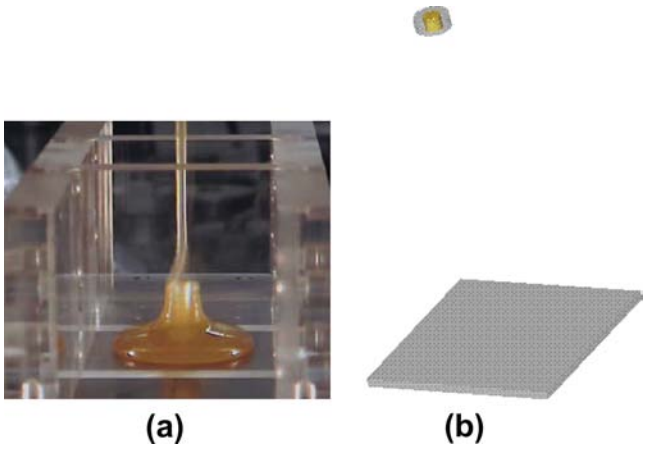

Fig. 12. (a) Jet buckling phenomenon [25]; (b) domain used in the simulation: jet diameter $D = 6$ mm, h' of the inlet to the plate $H = 12$ cm ($H/D = 20$).

To simulate this problem with the log-conformation tensor we employed the domain shown in Fig. 7. We considered an empty pipe where at its entrance (yellow[1] surface shown in Fig. 7) a fully developed velocity profile given by Eq. (26) was imposed. On the fluid free surface the full free surface stress conditions (see Eqs. (12)–(14)) were applied (for details see Tomé et al. [38]), while on the pipe walls the velocity obeyed the no-slip condition. At the outflow (pink surface shown in Fig. 7) homogeneous Neumann conditions were applied. The velocity and length scales used to determine the Reynolds and Weissenberg numbers and to present dimensionless quantities are the bulk velocity at the inlet pipe and its radius, respectively.

To verify the convergence of the log-conformation code on time-dependent problems we simulated the extrudate swell problem on three meshes with different levels of refinement for $Re = \frac{\rho UR}{\mu} = 0.5$ and $Wi = \lambda \frac{U}{R} = 0.3$. The mesh spacing employed were the same used in meshes **M1**, **M2**, **M3** defined in the previous section. Fig. 8 displays the results obtained on meshes **M1**, **M2**, **M3** at dimensionless times $t = 11$, 13.5 and 16. We can observe that as the mesh is refined the results obtained on meshes **M1** and **M2** approach those obtained on mesh **M3**. These results show that the log-conformation tensor is convergent on transient problems and spatially accurate.

To demonstrate that the log-conformation tensor technique can cope with highly elastic fluids we performed nine simulations of the time-dependent extrudate swell for increasing values of the Weissenberg number, namely, $Wi = 0.5, 0.8, 1, 1.25, 1.5, 1.75, 2, 2.3$ and 2.5, respectively. In these runs, a uniform mesh with spacing $\delta = 1/8$ (mesh **M1** used in Section 4) was employed. The results obtained for $Wi = 0.5, 1, 1.5, 2, 2.5$ are displayed in 3D views in Fig. 9. Fig. 9 displays the dynamics of the jets flowing inside the pipe and then being extruded into the air. For $t \geqslant 12$ all jets have

[1] For interpretation of colour in Figs. 1–14, the reader is referred to the web version of this article.

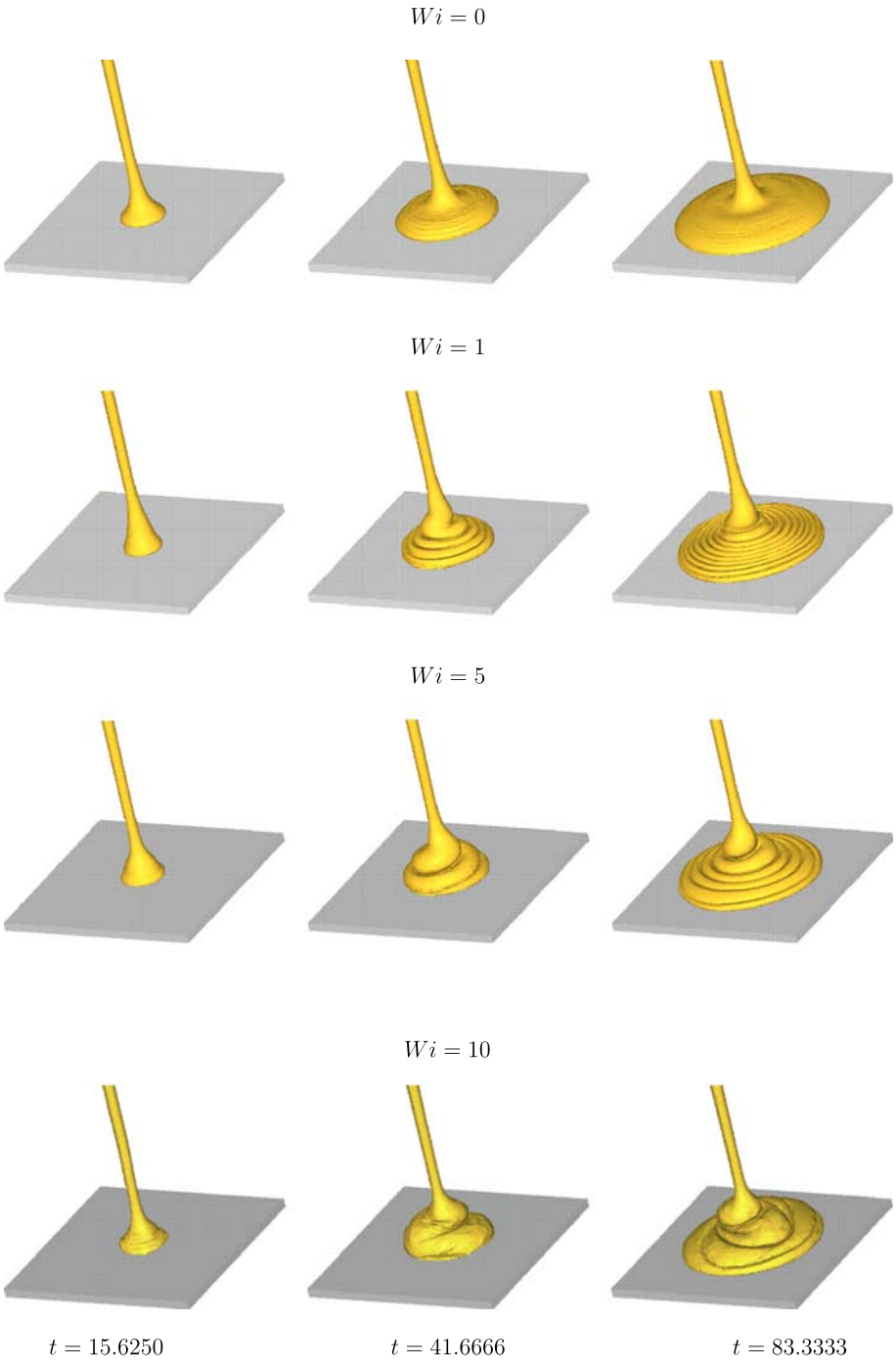

Fig. 13. Numerical simulation of time dependent jet buckling phenomenon using the log-conformation technique. UCM fluid, $Re = 1.5$,$Wi = 1, 5, 10, 20, 50$. Fluid flow visualisation at dimensionless times $t = t^* \frac{U}{D} = 15.6250, 41.6666, 83.3333$.

already exited the pipe and flow into the atmosphere. It can be seen that the jet with $Wi = 0.5$ progresses faster than the other jets with higher Wi; this is so because as Wi increases the swell produced becomes bigger and consequently the front moves slower due to mass conservation. At a later time, $t = 30$, we observe that all jets have been extruded into the air and the differences in the jet swells are more noticeable.

The swelling ratios, defined as the ratio between the maximum radius of the jet and the tube radius ($Sr = R_{max}/R$), obtained from these simulations are shown in Table 2 and plotted in Fig. 10, where we can observe an essentially linear variation of Sr with Wi. This constrast with the nonlinear behaviour of Tanner's law [35,36]

$$Sr = 0.13 + \left[1 + \frac{1}{2}\left(\frac{N_1}{T_{rz}}\right)_w^2\right]^{1/6} = 0.13 + [1 + 8Wi^2]^{1/6}, \quad (30)$$

the outcome of an approximate analysis of Tanner [35,36] which is also plotted in Fig. 10 for comparison purposes. In Eq. (30), the first normal stress difference, N_1, and the shear stress T_{rz} are evaluated at wall conditions pertaining to fully developed flow. We can see that for low Weissenberg numbers the agreement between the log-conformation tensor results and Tanner's predictions is very good, but differences increase progressively with Weissenberg number and these can be attributed to the fact that Tanner's law was obtained using an approximate analysis of the complex flow through the exit

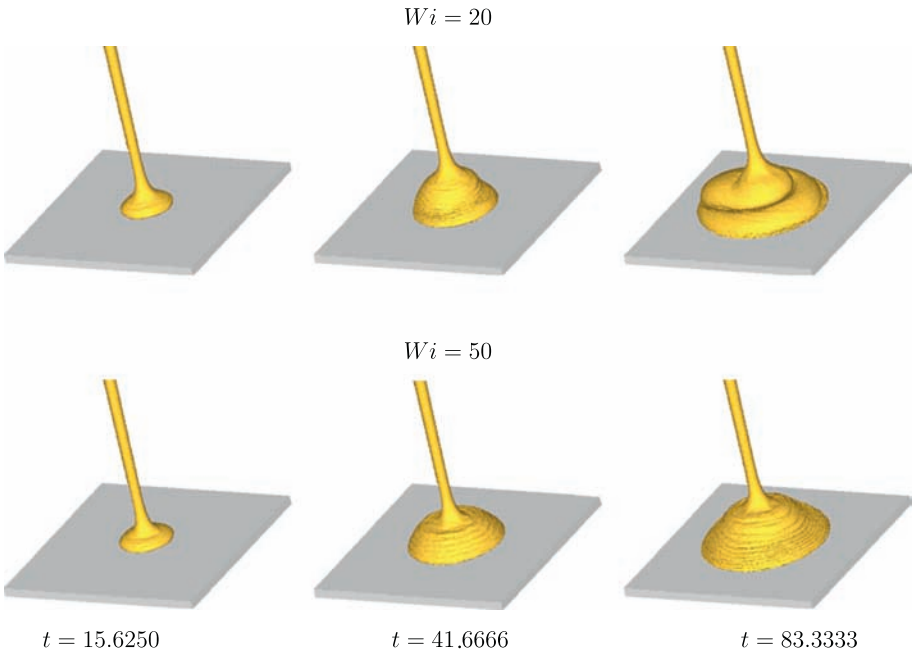

Fig. 13 (*continued*)

of the pipe together with the assumption of creeping flow ($Re = 0$) with a very long die, which is not the case in these numerical simulations on a not too fine mesh. Overall, and taking the different flow conditions into consideration, Fig. 10 displays a good qualitative agreement with Tanner's law.

To provide additional assurance to the results obtained with the log-conformation tensor, we considered the case $Wi = 1.5$ and performed two more simulations of the extrudate swell using meshes **M2** and **M3** of Section 4 with mesh spacings $\delta = 1/10$ and $\delta = 1/12$, respectively. The fluid surfaces obtained in these simulations at nondimensional times $t = 12, 17, 22$ are displayed in Fig. 11 where it can be seen that the fluid surfaces obtained on meshes **M1** and **M2** agree well with the fluid surface calculated on mesh **M3**. These results attest the correctness of the log-conformation tensor in obtaining the die-swell ratios obtained in the simulations performed by the Freeflow3D code.

We point out that no existing numerical algorithm has been able to predict die-swell of UCM fluids for very large Weissenberg numbers, especially transient three-dimensional flows. So far, these approaches have not used the log-conformation technique. For instance, Crochet and Keunings [12] used a finite element numerical method and reported results for the die-swell of a UCM fluid for Wi up to 2/3. More recently, Russo and Phillips [34] employed a spectral element to simulate two-dimensional die-swell of UCM fluids and reported results for Wi up to 1 while by using the log-conformation tensor, Choi and Hulsen [8] employed the log-conformation tensor to simulate 2D extrudate swell of UCM fluids and obtained results for Wi up to 1.5.

We therefore conclude that the only reason for our numerical technique to be able to predict extrudate swell for Wi up to 2.5 is essentially because of the log-conformation technique which made the numerical method more robust and more stable. According to Fattal and Kupferman [17], the log-conformation transformation allows a better description of the near-exponential stress growths in flows where advection and the Oldroyd derivative are important. In summary, the results presented in this section confirm that the log-conformation tensor approach can indeed accurately simulate flows of highly elastic fluids. In this work we were able to obtain converged solutions up to $Wi = 2.5$. In constrast, with the finite difference method based on the extra-stress tensor (see Tomé et al. [37]) the maximum Weissenberg number attained was only 0.4, beyond which the numerical method diverged.

5.2. Simulation of jet buckling of viscoelastic fluids

When a viscous jet flows onto a flat surface then under certain circumstances the phenomenon known as "jet buckling" can occur (see Fig. 12a). This is a physical fluid instability which has attracted the attention of many researchers (e.g. [14,15,31–33,37–39,41]). For Newtonian fluids, experimental and theoretical analyses (see Cruickshank and Munson [14]) show that a necessary condition for an axisymmetric jet undergo buckling is

$$Re \leqslant 1.2, \tag{31}$$

where Re is the Reynolds number which is calculated based on the inlet diameter (D), inlet velocity (U), fluid density (ρ) and fluid viscosity (η_0). With regard to viscoelastic fluids, a similar analysis providing conditions for the buckling of viscoelastic jets has not yet been reported. Notwithstanding, we will show that an increase in viscoelasticity (which is represented by the Weissenberg number, also based on the same velocity and length scales as the Reynolds number) makes an impinging jet more viscous (due to an increase of the extensional viscosity) so that radial flow resistance increases and eventually the jet undergoes buckling.

To demonstrate that viscoelasticity can induce jet buckling, we applied the log-conformation tensor technique to simulate the flow produced by a fluid jet modelled by the UCM constitutive equation. We considered a jet issued from an inlet positioned above a flat surface that flows vertically down onto it (see Fig. 12b) under the influence of gravity so that we had $Fr = \frac{U}{\sqrt{Dg}} = 2.0609$ and $Re = \frac{\rho UD}{\eta_0} = 1.5$. We anticipate that, since condition (31) is not satisfied, the corresponding Newtonian jet will not buckle. To observe the effect of viscoelasticity, the Weissenberg numbers employed in the simulations were $Wi = \frac{\lambda U}{D} = 0.5, 1, 5, 2, 10, 20, 50$. For comparison, the case of a Newtonian fluid ($Wi = 0$) was also simulated using the extra-stress methodology.

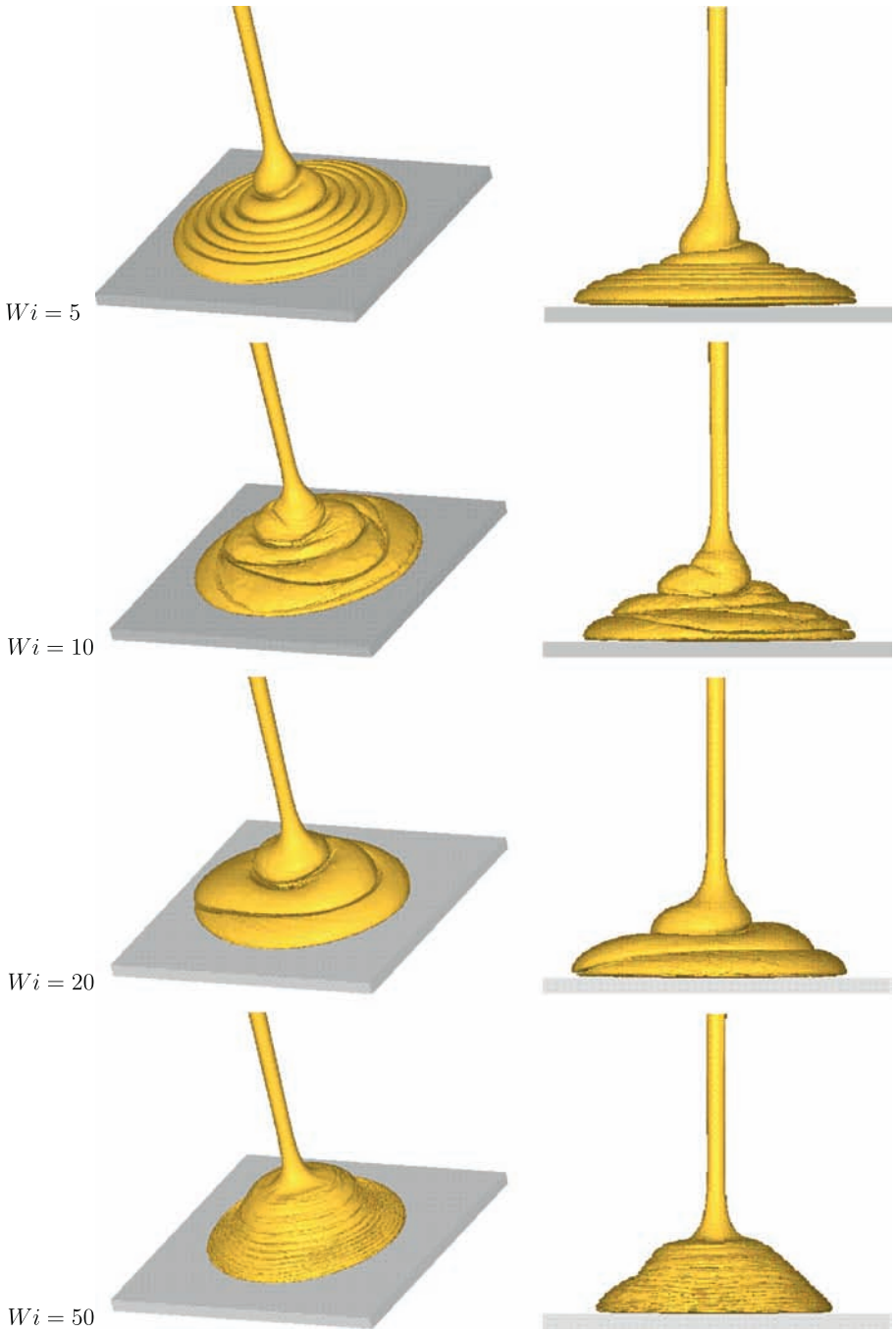

Fig. 14. Numerical simulation of time dependent jet buckling of an UCM fluid using the log-conformation technique with Re = 1.5. Fluid flow visualisation at dimensionless time $t = t^* \frac{U}{D} = 104.1666$ for increasing values of the Weissenberg number. Three-dimensional view (on the left) and frontal view (on the right).

The results obtained in these simulations are displayed in Figs. 13 and 14. As it was expected, we can observe in Fig. 13 that the Newtonian jet did not show any sign of buckling, in accordance with the analysis of Cruickshank and Munson [14]. However, all the UCM fluid jets exhibited buckling. We can note in Figs. 13 and 14 that as the Weissenberg number increases the jet becomes more viscous leading to slower radial flow. This behaviour is probably due to an increase of the elongational viscosity when Wi increases, especially in the region of impact, where a significant extensional component of the rate of deformation tensor is present and consequently the jet buckles. This fact has been demonstrated by Paulo et al. [28] who employed the Phan-Thien-Tanner model to simulate the jet buckling problem.

6. Concluding remarks

This paper reports an application of the log-conformation tensor technique to solve three-dimensional free surface flows governed by the UCM constitutive equation. The basic equations arising from the log-conformation transformation were presented and implemented in a three-dimensional viscoelastic code. The momentum equations were solved by the finite difference method presented by Tomé et al. [37]. The log-conformation equation was also approximated by the finite difference method on a staggered grid. The resulting code was applied to simulate the time-dependent extrudate swell of UCM fluids and results were obtained for Weissenberg numbers up to Wi = 2.5. The swelling ratios obtained

in these simulations for $Re = 0.5$ vary linearly with Wi in constrast with the approximate nonlinear theory of Tanner [35,36] for extrudate swell downstream a very long pipe under viscoleastic creeping flow conditions. Nevertheless, at low Weissenberg numbers the predictions agree well with Tanner's law. Moreover, the log-conformation tensor technique was applied to simulate jet buckling of UCM fluids for high Weissenberg numbers. The results showed that for small Wi the buckling was similar to that seen with low Reynolds number Newtonian jets. However, as the Weissenberg number was increased, the UCM jet became more viscous near the stagnation point and at $Wi = 50$, the buckling phenomenon was suppressed by a pyramid like structure which was formed by the impinging jet.

We note that the UCM3D solver of Tomé et al. [37] was only able to simulate the extrudate swell problem for $Wi \leqslant 0.4$ while for the jet buckling phenomenon, the maximum Weissenberg number achieved was $Wi = 0.6$. Therefore, a significant increase in the maximum Wi was obtained by the inclusion of the log-conformation tensor technique into the UCM3D solver of Tomé et al. [37] for three-dimensional time-dependent free surface flows governed by the UCM constitutive equation.

Acknowledgements

The support from the Brazilian funding agencies CNPq – Conselho Nacional de Desenvolvimento Científico e Tecnológico (Grants Nos. 302631/2010-0, 471793/2010-8, and 301408/2009-2) and CAPES (Grants Nos. BEX 4897/09-9 and BEX 2844/10-9) is gratefully acknowledged. This work is part of the activities developed in the Center for Mathematical Sciences Applied to Industry-CeMEAI and also benefits from the early collaboration within the framework of the University of São Paulo (Brazil) and University of Porto (Portugal) research agreements .

References

[1] A. Afonso, P.J. Oliveira, F.T. Pinho, M.A. Alves, The log-conformation tensor approach in the finite-volume method framework, J. Non-Newton. Fluid Mech. 157 (2009) 55–65.
[2] M. Alves, P. Oliveira, F. Pinho, A convergent and universally bounded interpolation scheme for the treatment of advection, Int. J. Numer. Method Fluids 41 (2003) 47–75.
[3] A. Afonso, F.T. Pinho, M.A. Alves, The kernel-conformation constitutive laws, J. Non-Newton. Fluid Mech. 167–168 (2012) 30–37.
[4] G.K. Batchelor, An Introduction to Fluid Dynamics, Cambridge University Press, 1967.
[5] M.G.H.M. Baltussen, M.A. Hulsen, G.W.M. Peters, Numerical simulation of the fountain flow instability in injection molding, J. Non-Newton. Fluid Mech. 165 (2009) 631–640.
[6] A. Castelo, M.F. Tomé, C.N.L. Cesar, J.A. Cuminato, S. McKee, Freeflow: an integrated simulation system for three-dimensional free surface flows, J. Comput. Vis. Sci. 2 (2000) 199–210.
[7] J.R. Clermont, M. Normandin, Numerical simulation of extrudate swell for Oldroyd-B fluid using the stream-tube analysis and a streamline approximation, J. Non-Newton. Fluid Mech. 50 (1993) 193–215.
[8] Y.J. Choi, M.A. Hulsen, Simulation of extrudate swell using an extended finite element method, Korea-Aust. Rheol. J. 23 (2011) 147–154.
[9] A. Chorin, Numerical solution of the Navier–Stokes, Maths. Comput. 2 (1968) 745–762.
[10] O.M. Coronado, D. Arora, M. Behr, M. Pasquali, A simple method for simulating general viscoelastic fluid flows with an alternate log-conformation formulation, J. Non-Newton. Fluid Mech. 147 (2007) 189–199.
[11] J. Cormenzana, A. Ledda, M. Laso, B. Debbaut, Calculation of free surface flows using CONNFESSITT, J. Rheol. 45 (2001) 237–258.
[12] M.J. Crochet, R. Keunings, Die swell of a Maxwell fluid: numerical prediction, J. Non-Newton. Fluid Mech. 7 (1980) 199–212.
[13] M.J. Crochet, R. Keunings, Finite element analysis of die-swell of a highly elastic fluid, J. Non-Newton. Fluid Mech. 10 (1982) 339–356.
[14] J.O. Cruickshank, B.R. Munson, Viscous-fluid buckling of plane axisymmetric jets, J. Fluid Mech. 113 (1981) 221–239.
[15] J.O. Cruickshank, Low-Reynolds-number instabilities in stagnating jet flows, J. Fluid Mech. 193 (1988) 111–127.
[16] H. Damanik, J. Hron, S. Turek, A monolithic FEM approach for the log-conformation reformulation (LCR) of viscoelastic flow problems, J. Non-Newton. Fluid. Mech. 165 (2010) 1105–1113.
[17] M.M. Denn, Extrusion instabilities and wall slip, Ann. Rev. Fluid Mech. 33 (2001) 265–287.
[18] R. Fattal, R. Kupferman, Constitutive laws for the matrix-logarithm of the conformation tensor, J. Non-Newton. Fluid. Mech. 123 (2004) 281–285.
[19] G.C. Georgiou, W.W. Schultz, Olson, Singular finite elements for the sudden-expansion and the die-swell problems, Int. J. Numer. Method Fluids 10 (1990) 357–372.
[20] J.I. Guermond, I. Quatapelle, On the approximation of the unsteady Navier–Stokes equations by finite element projection methods, Numer. Math. 80 (1998) 207–238.
[21] M.A. Hulsen, R. Fattal, R. Kupferman, Flow of viscoelastic fluids past a cylinder at high Weissenberg number: stabilized simulations using matrix logarithms, J. Non-Newton. Fluid Mech. 127 (2005) 27–39.
[22] V. Legat, J.M. Marchal, Die design: an implicit formulation for the inverse problem, Int. J. Numer. Method Fluids 16 (1993) 29–42.
[23] Y. Kwon, Finite element analysis of planar 4:1 contraction flow with the tensor logarithmic formulation of differential constitutive equations, Korea-Aust. Rheol. J. 16 (2004) 183–191.
[24] V. Ngamaramvaranggul, W.F. Webster, Viscoelastic simulations of stick-slip and die-swell flows, Int. J. Numer. Method Fluids 36 (2001) 539–595.
[25] J.M. Nobrega, O.S. Carneiro, F.T. Pinho, G.S. Paulo, M.F. Tomé, A. Castelo, J.A. Cuminato, The phenomenon of jet buckling: experimental and numerical predictions, in: Proceedings of The Polymer Processing Society 23rd Annual Meeting, Guimarães, Portugal, 2007.
[26] R.G. Owens, T.N. Phillips, Computational Rheology, Imperial College Press., London, 2002.
[27] T.-W. Pan, J. Hao, R. Glowinski, On the simulation of a time-dependent cavity flow of an Oldroyd-B fluid, Int. J. Numer. Method Fluids 60 (2009) 791–808.
[28] G.S. Paulo, M.F. Tomé, S. McKee, A marker-and-cell approach to viscoelastic free surface flows using the PTT model, J. Non-Newton. Fluid Mech. 147 (2007) 149–174.
[29] W.H. Press, B.P. Flannery, S.A. Teukolsky, W.T. Vetterlin, Numerical Recipes in FORTRAN, Cambridge University Press, 1988.
[30] D. Rajagopalan, R. Amstrong, R. Brown, Finite element methods for calculation of steady viscoelastic flow using constitutive equations with newtonian viscosity, J. Non-Newton. Fluid. Mech. 36 (1990) 159–192.
[31] N.M. Ribe, A general theory of the dynamics of thin viscous sheets, J. Fluid Mech. 457 (2002) 255–283.
[32] N.M. Ribe, Periodic folding of viscous jets, Phys. Rev. E. 68 (2003) (Art. No. 036305 Part).
[33] N.M. Ribe, Coiling of viscous jets, Proc. Roy. Soc. Lond. Ser. A – Math. Phys. Eng. Sci. 460 (2004) 3223–3239.
[34] G. Russo, T.N. Phillips, Spectral element predictions of die-swell for Oldroyd-B fluids, Comput. Fluids 43 (2011) 107–118.
[35] R.I. Tanner, A theory of die-swell, J. Polm. Sci. 8 (1970) 2067–2078.
[36] R.I. Tanner, A theory of die-swell revisited, J. Non-Newton. Fluid Mech. 129 (2005) 85–87.
[37] M.F. Tomé, R.A. Pimentel, C.M. Oishi, S. McKee, Numerical solution of the Upper-Convected Maxwell model for three-dimensional free surface flows, Commun. Comput. Phys. 6 (2009) 367–395.
[38] M.F. Tomé, A. Castelo, V.G. Ferreira, S. McKee, A finite difference technique for solving the Oldroyd-B model for 3D-unsteady free surface flows, J. Non-Newton. Fluid. Mech. 154 (2008) 179–206.
[39] M.F. Tomé, A. Castelo, J.A. Cuminato, N. Mangiavacchi, S. McKee, GENSMAC3D: a numerical method for solving unsteady three-dimensional free surface flows, Int. J. Numer. Method Fluids 37 (2001) 747–796.
[40] M.F. Tomé, S. McKee, GENSMAC: a computational marker-and-cell method for free surface flows in general domains, J. Comput. Phys. 110 (1994) 171–186.
[41] L. Ville, L. Silva, T. Coupez, Convected level set method for the numerical simulation of fluid buckling, Int. J. Numer. Method Fluids 66 (2011) 324–344.